



Effect of Film Thickness on the Microstructure and Dielectric and Ferroelectric Properties of $(\text{Bi}_{0.5}\text{Na}_{0.5})_{0.94}\text{Ba}_{0.06}\text{TiO}_3$ Films by Pulsed Laser Deposition

Lin Li^{1,2,3} · Changrong Zhou^{2,3} · Dongyan Yu¹ · Yuanlei Zheng^{1,2,3} · Yusong Du^{2,3} · Lei Ma^{2,3} · Jingtai Zhao^{1,2,3} · Guanghui Rao^{1,2,3}

Received: 26 September 2022 / Accepted: 20 February 2023 / Published online: 13 March 2023
© The Minerals, Metals & Materials Society 2023

Abstract

Lead-free $(\text{Bi}_{0.5}\text{Na}_{0.5})_{0.94}\text{Ba}_{0.06}\text{TiO}_3$ (BNT-6BT) films are deposited on Pt(111)/Ti/SiO₂/Si(100) substrates for various thicknesses by pulsed laser deposition. The effects of thickness on the microstructure, Raman spectra, dielectric behavior, and ferroelectric properties are investigated in detail. The BNT-6BT films with a polycrystalline structure, as well as an increase in grain size and crystallinity, a decrease in strain, and the appearance of columnar crystals with increasing film thickness are confirmed by x-ray diffraction and field emission scanning electron microscopy. Obvious aging behavior with an abnormal double-butterfly shape of dielectric constant–electric field curves is observed in aged BNT-6BT films. Both the dielectric tunability and dielectric constant increase with increasing film thickness, with 950 nm film exhibiting the highest dielectric tunability of 36.7% and dielectric constant and loss of 572 and 0.032 at 1 kHz, respectively. Moreover, an increase in the maximum polarization (P_{max}) and remanent polarization (P_r) with the increase in film thickness is also observed. The enhanced dielectric and ferroelectric properties of BNT-6BT films are strongly depended on thickness, which suggest the potential application of BNT-6BT films in film tunable capacitors.

Keywords BNT-6BT films · pulsed laser deposition · defect dipoles · aging effect · dielectric behavior

Introduction

$(\text{Bi}_{0.5}\text{Na}_{0.5})\text{TiO}_3$ (BNT) ferroelectric offers multiple advantages in microelectronic applications and microelectromechanical systems (MEMS) to replace lead-based compounds due to its outstanding electrical properties, with large remanent polarization ($P_r \sim 38 \mu\text{C}/\text{cm}^2$), high coercive

field ($E_c \sim 73 \text{ kV}/\text{cm}$), and relative high Curie temperature (320°C).¹ In particular, the morphotropic phase boundary (MPB) composition $(\text{Bi}_{0.5}\text{Na}_{0.5})_{1-x}\text{Ba}_x\text{TiO}_3$ (BNT-BT) with rhombohedral and tetragonal phase coexistence presents excellent ferroelectric, piezoelectric, and dielectric properties.^{2,3} Nevertheless, for BNT or BNT-based solid solutions, especially in the form of thin films, the fabrication and characterization are still hot topics.^{4–6} MPB composition of BNT-BT is characterized by large electrical hysteresis and high leakage current during the poling process, which may limit some of their applications. To date, considerable efforts have been made to overcome the adverse effects of cation volatilization for BNT and BNT-based films.^{7–10} However, the fabrication of high-quality pure BNT-based films with tunable thickness remains a challenging task. Among film fabrication methods, pulsed laser deposition (PLD) technology is suitable for the synthesis of high-quality stoichiometric multicomponent oxide films, due to the highly supersaturated ablation plasma plume, the adjustable deposition rate, and the high uniformity attainable by optimizing various deposition parameters including laser energy density, laser

✉ Changrong Zhou
zcr750320@guet.edu.cn

✉ Guanghui Rao
rgh@guet.edu.cn

¹ School of Mechanical and Electrical Engineering, Guilin University of Electronic Technology, Guilin 541004, Guangxi, China

² School of Materials Science and Engineering, Guilin University of Electronic Technology, Guilin 541004, Guangxi, China

³ Guangxi Key Laboratory of Information Materials, Guilin University of Electronic Technology, Guilin 541004, Guangxi, China

repetition rate, background reactive gas pressure, substrate temperature, and target-to-substrate distance, resulting in single, stoichiometric, and homogeneous film.^{11,12}

For designing a device based on ferroelectric films, it is essential to investigate the thickness-dependent microstructure and electrical properties of the films. For instance, ferroelectricity may be lost below a critical thickness or critical volume. Dielectric properties also typically degrade with decreasing thickness.¹³ However, most previous works investigating thickness-dependent behavior have focused on other systems, such as Pb (Zr,Ti)O₃ (PZT),^{14,15} BiFeO₃ (BFO).^{16,17} Only a few reports involve the study of the thickness dependence of BNT-based films. Yang et al. prepared Na_{0.5}Bi_{0.5}(Ti,Zn)O_{3-δ} films with various single-coated layer thicknesses, where the film of 20 nm per layer (nm/l) with a typical columnar structure exhibited superior dielectric properties, with tunability of 43.2% at 240 kV/cm and 100 kHz.¹⁸ With the thickness of 0.8(Bi_{0.5}Na_{0.5})TiO₃-0.2SrTiO₃ films increasing from 150 nm to 210 nm, enhanced ferroelectricity and piezoresponse were achieved due to thermally driven stress.¹⁹ As for the pure BNT films deposited by PLD with thickness of 208–1300 nm, the microwave dielectric and nonlinear optical properties of BNT films were strongly dependent on thickness, i.e., the dielectric constant (ϵ_r) obviously increased with the film thickness, while the nonlinear optical properties gradually decreased.²⁰ In this paper, MPB composition (Bi_{0.5}Na_{0.5})_{0.94}Ba_{0.06}TiO₃ (BNT-6BT) ferroelectric films with different thicknesses on Pt(111)/Ti/SiO₂/Si(100) substrates were prepared by pulsed laser deposition; the microstructure, dielectric behavior, and ferroelectric properties were systematically investigated.

Experimental Procedure

The BNT-6BT thin films were deposited on Pt(111)/Ti/SiO₂/Si(100) substrates by PLD with a KrF excimer laser (248 nm). The stoichiometric (Bi_{0.5}Na_{0.5})_{0.94}Ba_{0.06}TiO₃ ceramic targets were prepared by solid-state reaction using Na₂CO₃, BaCO₃, TiO₂, and Bi₂O₃ powders and sintering at 1150°C for 2 h. During the laser ablation process, laser energy density of 2 J/cm² with repetition frequency of 10 Hz was used. The BNT-6BT films were deposited at a substrate temperature of 675°C under oxygen partial pressure of 30 Pa. After deposition, in situ annealing was carried out in a 1 atm oxygen atmosphere for 30 min to reduce oxygen deficiencies.

The crystal structure of the BNT-6BT films was studied by x-ray diffraction (XRD) with Cu-K α_1 radiation ($\lambda = 1.5406 \text{ \AA}$) (Empyrean PIXcel^{3D}, PANalytical, Netherlands). The surface morphology and thickness were examined by field emission scanning electron microscopy (FESEM) (FEG 450, FEI, USA) and atomic force

microscopy (AFM) (MultiMode-8, Bruker, USA). The Raman spectra were examined by Raman spectroscopy (LabRAM HR Evolution, HORIBA, France). X-ray photoelectron spectroscopy (XPS) (ESCALAB 250Xi, Thermo Fisher, USA) was used to analyze the chemical bonding states. The Au top electrodes with a diameter of 0.6 mm were prepared using DC sputtering for electrical measurement. The ferroelectric hysteresis loops and dielectric behavior were measured using a ferroelectric testing system (TF 2000 analyzer, aixACCT, Germany) and impedance analyzer (E4294, Agilent, USA), respectively.

Results and Discussion

Figure 1a illustrates the XRD patterns of BNT-6BT thin films with various thicknesses from 150 nm to 950 nm. All diffraction peaks can be indexed and are in good agreement with those of the standard diffraction peaks (Bi_{0.5}Na_{0.5})TiO₃ (*PDF* = 01-089-3109), suggesting a pure BNT pseudocubic perovskite structure without secondary phases and a polycrystalline structure with no apparent preferential orientation. Furthermore, Fig. 1b shows the enlarged XRD pattern of the (110) peak in the vicinity of 32°. The result displays a slight offset towards lower angles of the (110) diffraction peak with increasing film thickness, which may be due to an increase in the lattice constant. Also, the full width at half maximum (FWHM) of the (110) peak decreases with an increase in film thickness, suggesting enhanced crystallinity of the BNT-6BT films.

The XRD pattern can also be utilized to evaluate peak broadening with crystallite size and lattice strain due to dislocation. The crystallite sizes (*D*) and lattice strain (ϵ)

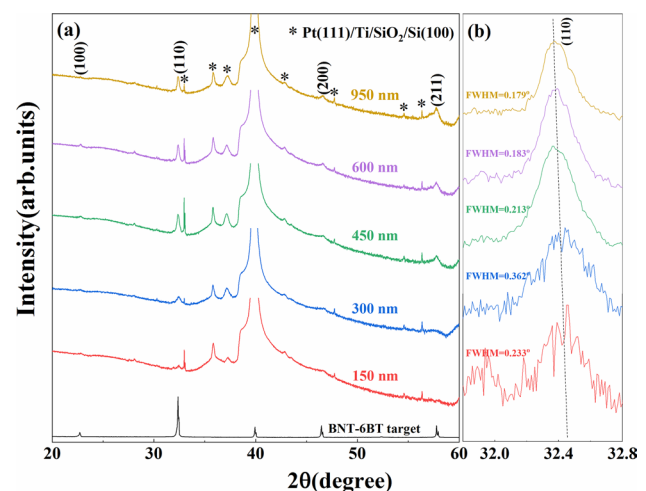


Fig. 1 (a) XRD pattern of BNT-6BT films with different thicknesses; (b) enlarged XRD pattern of (110) peak in the vicinity of 32°.

of films can be calculated by the Williamson–Hall (WH) equation,²¹

$$\beta_{hkl} \cos \theta = k\lambda/D + 4\varepsilon \sin \theta \quad (1)$$

where β_{hkl} is the full width of the diffraction peaks at half maximum (FWHM), θ is the diffraction angle, k is the shape factor (for spherical; $k=0.89$), λ is the wavelength of the radiation (for Cu- K_{α} ; $\lambda=1.5406 \text{ \AA}$), D is the average crystallite size, and ε is the strain of the films ($\Delta/l/l$). The W–H plots ($\beta_{hkl} \cos \theta$ versus $4\sin \theta$) are shown in Fig. 2. The intercept ($k\lambda/D$) on the $\beta_{hkl} \cos \theta$ axis and slope (ε) are given by linear fitting in the W–H plots. The values of D are estimated as 63 nm, 74 nm, 95 nm, and 116 nm for 300 nm, 450 nm, 600 nm, and 950 nm films, respectively. On increasing the film thickness, the crystallite size increases monotonically, which dominates the left shift of the diffraction peak. Moreover, the calculated values of ε are shown in Fig. 2 from the W–H plots, which suggests that the 300 nm film has higher strain than the 450 nm film. The 450 nm film exhibits the smallest strain of 0.0016 and then increases slightly with a further increase in thickness. The results are similar to those of a previous report of BNT films by PLD.^{20,22} Hence, the residual strain of the film may be another cause of peak shift, in that the shrinkage and expansion of the lattice would cause the peaks to shift right and shift left, which is

attributed to the compressive strain and tensile strain of the deposited films, respectively.²³ During the film deposition by PLD, the strain caused by the crystal distortion is inherently present in the films due to the difference in lattice constants between the film and the substrate.²⁴ At the early stage of film deposition, compressive strain is formed at the interface between the grown films (BNT-6BT) and the substrate and relaxed in the direction of film thickness. Then, with increasing thickness of the films, the strain is reduced to the lowest value at a critical thickness which is related to the quality of the film and the process conditions.²⁵ Hence, a critical thickness of 450 nm in BNT-6BT films is obtained and the residual tensile strain is enhanced with a further increase in thickness.²⁰ Moreover, lattice strain is a manifestation of the change in lattice constant caused by crystal defects, such as lattice dislocations, grain boundary triple junctions, inter-contact stress, stacking faults, and coherent stress.²⁶ It can be expected that the reduction of lattice strain of thin films will promote the growth of grains.

Figure 3a–e presents the surface and cross-sectional (inset) morphology of the BNT-6BT films with various thicknesses. All deposited films exhibit irregular grains with clear grain boundaries, which indicates good crystallization. The 150 nm and 300 nm films reveal a relatively dense surface structure, while some fine grain gaps are scattered on the film surface above the critical thickness

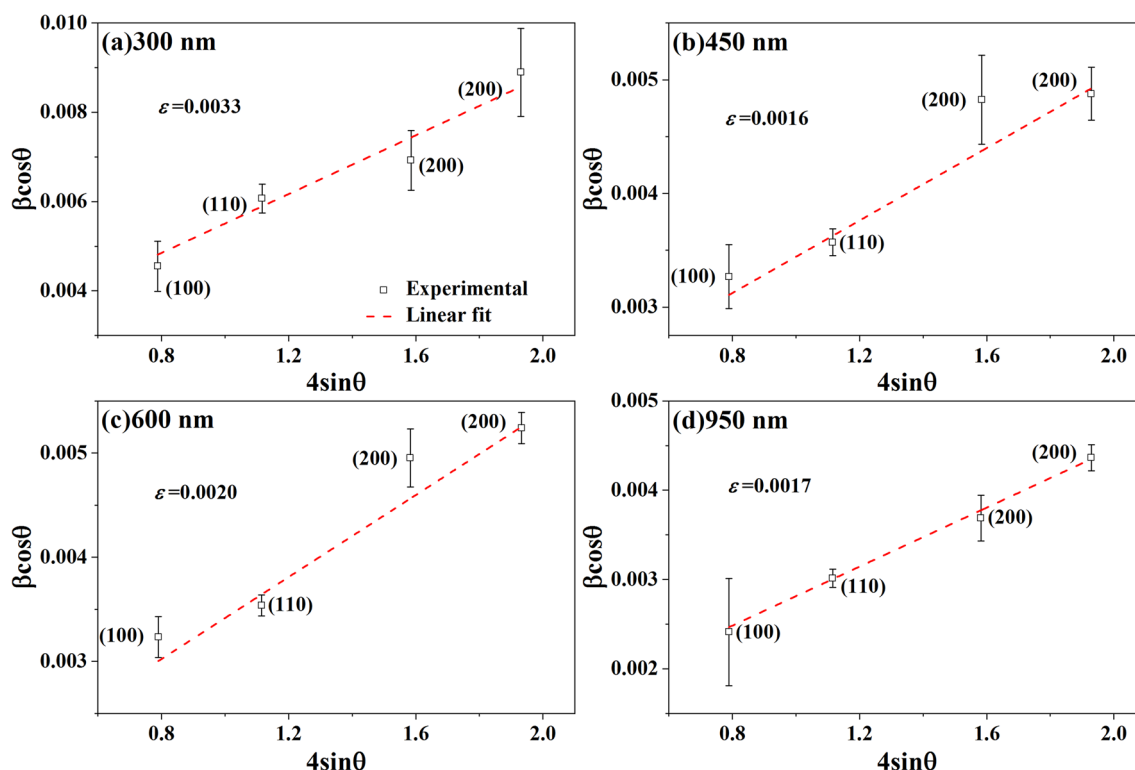


Fig. 2 W–H plots of BNT-6BT films for (a) 300 nm, (b) 450 nm, (c) 600 nm, and (d) 950 nm.

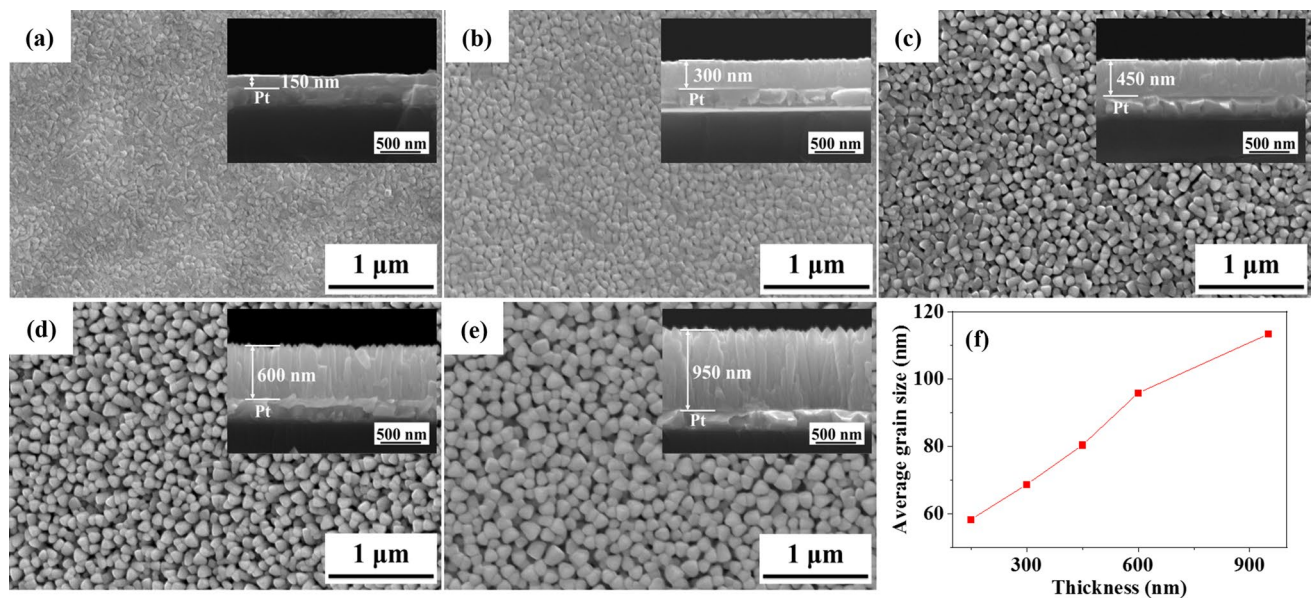


Fig. 3 FESEM surface morphology of BNT-6BT films for (a) 150 nm, (b) 300 nm, (c) 450 nm, (d) 600 nm, and (e) 950 nm. The inset shows the corresponding cross-sectional images. (f) The average grain size of BNT-6BT films with different thicknesses.

of 450 nm, which may be due to grain growth or volatilization of the A-site cation during the fabrication process.²⁷ The average grain size is calculated by measuring 100 randomly selected grains in the FESEM images. Values of 58.3 nm, 68.7 nm, 80.4 nm, 95.9 nm, and 113.4 nm are obtained for film thickness of 150 nm, 300 nm, 450 nm, 600 nm and 950 nm, respectively, which is consistent with the XRD results (crystallite size). Moreover, from the cross-sectional morphology, the grain growth by the formation of columnar grains along the thickness direction can be clearly observed with increasing thickness above 450 nm. Clearly, the grains of 450 nm film present two forms at the initial stage of columnar growth, as shown in Fig. 3c.

It is believed that the strain of films will be relieved by a series of misfit dislocations perpendicular to the substrate–film interface with increasing thickness. When the thickness exceeds the critical thickness, the introduced dislocation releases the strain energy of the film and induces pseudocrystalline growth.²⁴ The growth of columnar grains can be promoted due to minimum lattice strain and lower surface energy of the films deposited at high temperature.^{20,28} In addition, the surface morphological characteristics of FESEM images are consistent with the AFM images recorded over a $2 \times 2 \mu\text{m}^2$ scan region in Fig. 4. Root-mean-square (RMS) surface roughness values of 6.107 nm, 7.388 nm, 10.45 nm, 12.83 nm, and 23.71 nm are calculated for the deposited films with thickness of 150 nm, 300 nm, 450, 600 nm, and 950 nm, respectively. The increased roughness may be due to the formation and growth of columnar grains.

The structure and phase evolution of films can also be revealed by Raman spectroscopy due to its sensitivity to tiny changes in local structure over a short range.²⁹ The RT Raman scattering spectrum of BNT-6BT films with various thicknesses tested in the range of $100\text{--}1100 \text{ cm}^{-1}$ is shown in Fig. 5a. The experimental data were fitted by considering a Gaussian function, and six vibration modes are present for all films. The results for vibration modes and the full width at half maximum (FWHM) of various thicknesses of films are displayed in Fig. 5b and c. As stated by group theory, for BNT and BNT-based film, the vibration mode at a low wavenumber below 200 cm^{-1} (denoted as A) is related to stretching vibrations of A-site elements, such as Bi-O, Na-O, and Ba-O. The Raman wavenumber in the range of $200\text{--}400 \text{ cm}^{-1}$ (denoted as B) corresponds to Ti-O stretching vibration, and the vibration modes associated with the TiO_6 oxygen octahedral (denoted as C_1 , C_2 , C_3 , and C_4) are found at a higher wavenumber of the spectrum (above 400 cm^{-1}).^{30,31}

With increasing thickness, an obvious blue shift of A, B, C_1 , and C_2 modes towards the higher wavenumber and a gradual decrease in the FWHM at 450 nm are observed. When the thickness increases above 450 nm, a shift back to a lower wavenumber and a slight increase in the FWHM are seen. The decrease in the FWHM indicates an increase in crystallinity due to the decreased lattice distortion of the film.²⁰ The shift in the wavenumbers and the change in the FWHM of the vibration peaks directly reflect the subtle structural changes of the films and suggest the presence of MPB composition.³² Thus, the effect of strain variation within the films with different thicknesses can also be

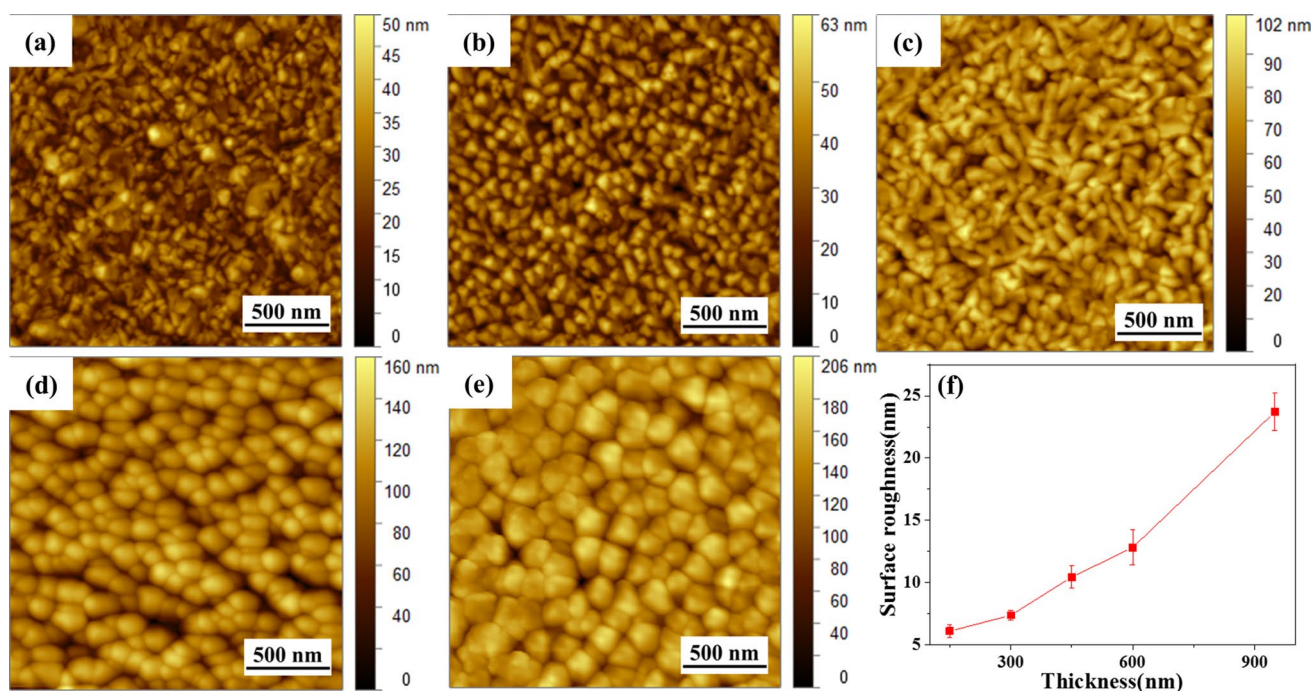
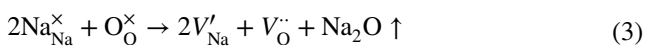
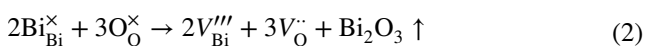


Fig. 4 AFM micrograph of the films recorded over a $2 \times 2 \mu\text{m}^2$ scan region for (a) 150 nm (b) 300 nm, (c) 450 nm, (d) 600 nm, and (e) 950 nm. (f) Surface roughness as a function of film thickness.

suggested. Raman spectroscopy results are consistent with XRD, FESEM, and AFM results.

It is known that the electrical properties of perovskite films are strongly affected by chemical defects.³³ In order to identify the chemical valence of the BNT-6BT film, x-ray photoelectron spectroscopy (XPS) studies were performed, and the results are displayed in Fig. 6.

The asymmetric XPS peaks are fitted by Gaussian–Lorentzian distributions. Three peaks can be fitted with O 1s spectra. The lower binding energy peak at 529.6 eV is associated with lattice oxygen, and includes Na–O, Ti–O, Bi–O, and Ba–O bonding.³⁴ The peaks at 531.5 and 531.3 eV are contributed by singly charged (V_{O}^{\cdot}) and doubly charged vacancies ($V_{\text{O}}^{\cdot\cdot}$), respectively.³⁵ The Ti 2p peaks at 457.9 eV and 458.4 eV are attributed to Ti^{3+} and Ti^{4+} , respectively.³⁶ Thus, the volatilization of the A-site cation during fabrication of BNT-based films leads to the formation of cation vacancies and oxygen vacancies ($V_{\text{O}}^{\cdot\cdot}$) By following Kröger–Vink notation,³⁷



On the other hand, the presence of Ti^{3+} ions at B-sites results in the nonequivalence of neighboring O^{2-} sites

because the charged Ti^{3+} ion is slightly displaced from Ti^{4+} sites.



Hence, the formation of V_{O}^{\cdot} or $V_{\text{O}}^{\cdot\cdot}$ occurs to compensate the overall charge neutrality.

The DC electric field dependence of the small-signal ϵ_r of the BNT-6BT films with various thicknesses measured under 1 kHz is shown in Fig. 7. The dielectric constant–electric field (ϵ_r – E) curves were tested by sweeping the DC voltage from a negative to a positive bias (up-sweep) and then sweeping back (down-sweep). All films show an abnormal ϵ_r – E curve with four peaks, which is an obvious feature of the aging phenomenon. Similar dielectric behavior has been reported in other systems, such as $\text{Na}_{0.5}\text{Bi}_{0.5}(\text{Ti}_{0.94}\text{Fe}_{0.06})\text{O}_{3-\delta}$ ³⁸ and BiFeO_3 – $\text{Na}_{0.5}\text{Bi}_{0.5}\text{TiO}_3$.³⁹ It has been confirmed that the aging behavior is a volume effect and strongly depends on the content of defect dipoles.⁴⁰ In the BNT-6BT films, the defect dipoles can be formed between acceptor cation defects $V_{\text{Na}}^{\prime}/V_{\text{Bi}}^{\text{'''}}$ or $\text{Ti}_{\text{Ti}^{4+}}^{(3+)}$ and oxygen vacancies V_{O}^{\cdot} or $V_{\text{O}}^{\cdot\cdot}$ based on the XPS analysis, such as $V_{\text{Na}}^{\prime}/V_{\text{Bi}}^{\text{'''}} - V_{\text{O}}^{\cdot}$, $\text{Ti}_{\text{Ti}^{4+}}^{(3+')} - V_{\text{O}}^{\cdot}$, and/or $\text{Ti}_{\text{Ti}^{4+}}^{(3+')} - V_{\text{O}}^{\cdot\cdot}$. The defect polarization (P_{D}) is constituted and gradually aligned along the spontaneous polarization (P_{S}) direction

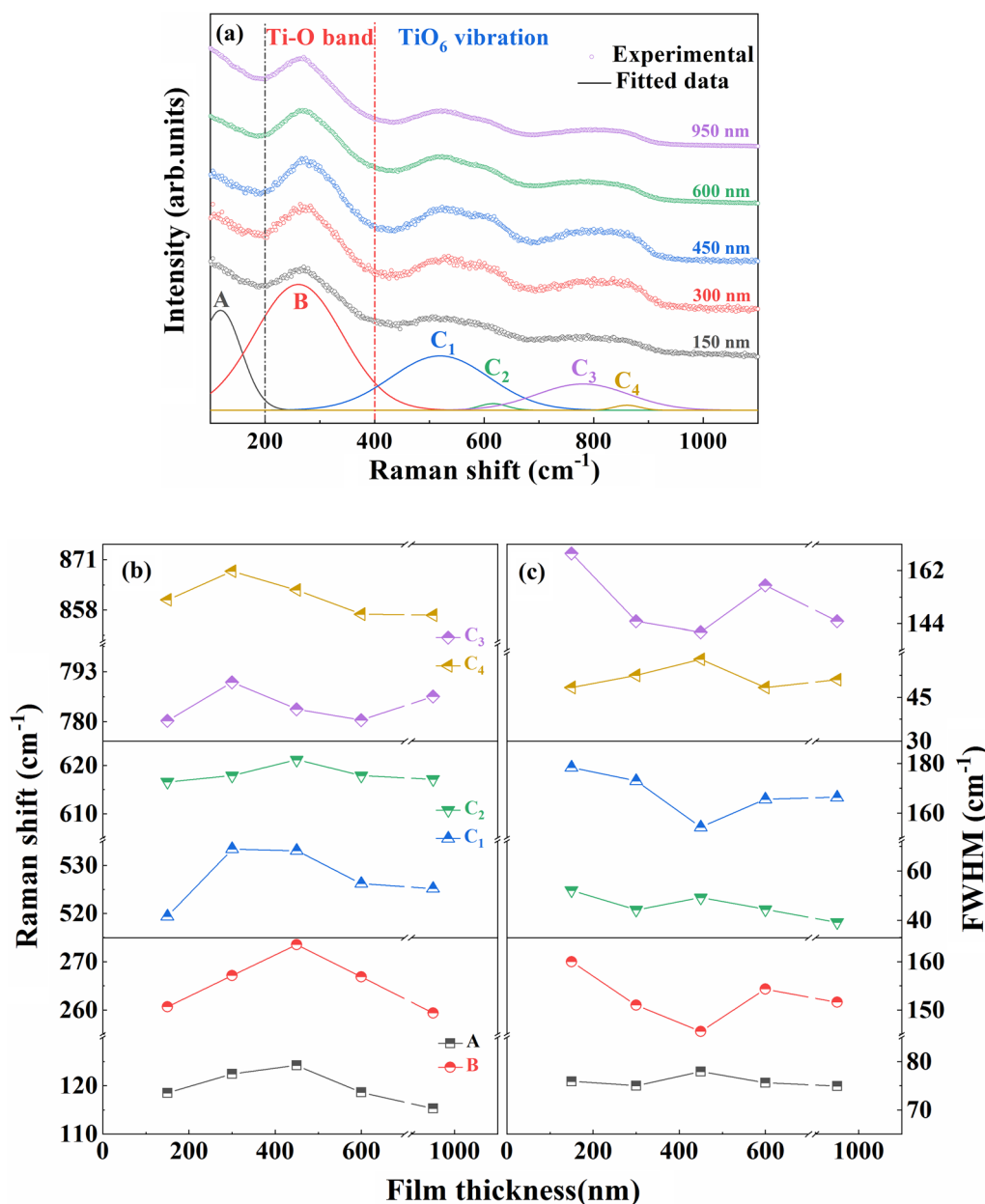


Fig. 5 (a) Room-temperature Raman spectra of BNT-6BT films. Thickness-dependent peak position (b) and FWHM (c) of the vibration modes for BNT-6BT films.

to fulfill the lowest energy principle during aging of films samples.⁴¹ When an electric field (E) is applied on the aged film, domain switching occurs, with P_s following the field direction, while the P_D remains in the original state because E is too low to overcome the electrostatic attraction force between the defect dipoles. After removing E , the P_D provides a restoring force to reverse the switched P_s to its original orientation.⁴² Thus, an abnormal double-butterfly-shaped loop with four peaks is observed. In addition, the electric field of the peak position in the ϵ_r - E curve decreases slightly with the film thickness, which can

be attributed to the increase in grain size with increasing thickness of the films, resulting in larger domain sizes.

Figure 8a shows the ϵ_r - E curve of BNT-6BT films under a down-sweeping DC electric field at 1 kHz. Clearly, all ϵ_r - E curves with a typical single-butterfly-type shape and strong field asymmetry are observed to shift towards the positive electric field. As discussed above, the emergence of the single-butterfly-type shape can be explained by the breaking of defect dipoles under the higher E , because the defect can obtain sufficient migration energy under a higher electric field.^{38,43} The asymmetry of the

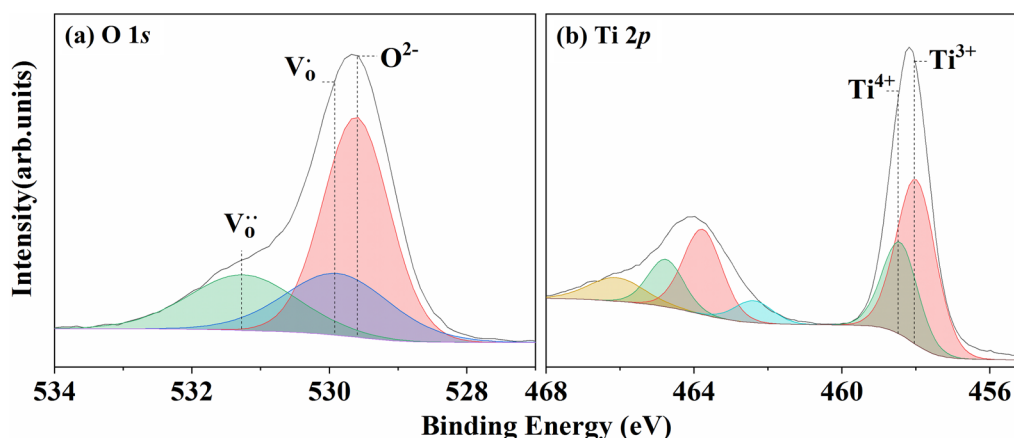


Fig. 6 (a) O 1s and (b) Ti 2p XPS spectra of BNT-6BT thin film with thickness of 450 nm.

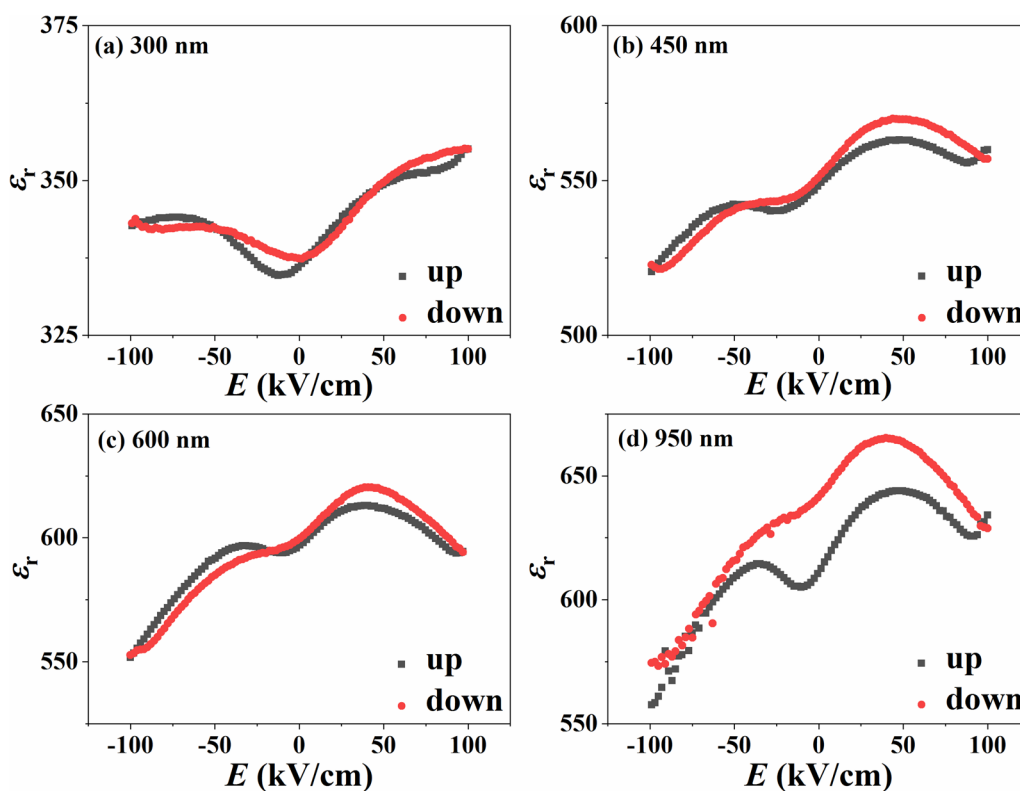


Fig. 7 The ϵ_r - E curves of BNT-6BT films with different thicknesses of (a) 300 nm, (b) 450 nm, (c) 600 nm, and (d) 950 nm.

ϵ_r - E curve may be related to point defects and domain wall pinning (freezing or clamping).⁴⁴ In addition, when E increases to 200 kV/cm, the strong reduction of ϵ_r can be evaluated by the dielectric tunability $\Delta\epsilon_r/\epsilon_{r0}$, where $\Delta\epsilon_r$ is the difference in the dielectric constant, and ϵ_{r0} is the dielectric constant without E . The tunability calculated at 200 kV/cm is tabulated in Table I, suggesting that increasing the thickness of films helps to improve the ϵ_r response

to the applied bias field. The RT dielectric constant (ϵ_r) and dielectric loss ($\tan \delta$) as a function of frequency were investigated in the range of 40 Hz to 200 kHz and are shown in Fig. 8b. The estimated ϵ_r and $\tan \delta$ values at 1 kHz are listed in Table I. All films exhibit frequency-dispersive behavior. Based on the XPS analysis and Kröger-Vink notation, the space charge would be trapped in $V'_{Na}/V'''_{Bi} - V_{O^{\bullet}}$, $Ti^{(3+)}_{Ti^{4+}} - V_{O^{\bullet}}$, and/or $Ti^{(3+)}_{Ti^{4+}} - V_{O^{\bullet}}$ defects,

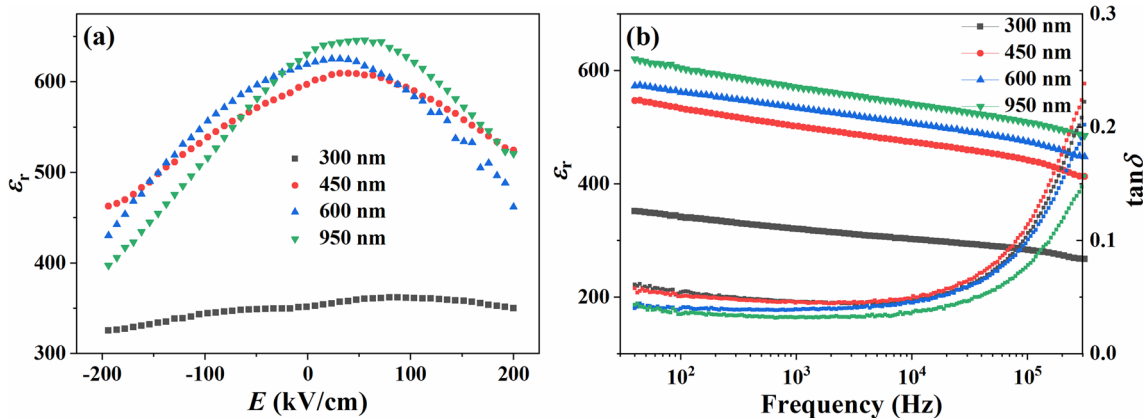


Fig. 8 (a) The dielectric constant (ϵ_r) with down-sweeping DC electric field and (b) dielectric constant (ϵ_r) and dissipation factor ($\tan \delta$) as a function of frequency for BNT-6BT films with different thicknesses.

Table I Thickness-dependent dielectric and ferroelectric properties of BNT-6BT films

Film thickness (nm)	ϵ_r @1 kHz	$\tan \delta$ @1 kHz	$\Delta\epsilon_r/\epsilon_{r0}$ (%)	P_{max} ($\mu\text{C}\cdot\text{cm}^{-2}$)	P_r ($\mu\text{C}\cdot\text{cm}^{-2}$)
300	320	0.046	7.6	10.06	1.76
450	502	0.045	23.1	19.55	6.78
600	534	0.039	32.3	23.44	5.72
950	572	0.032	36.7	25.19	8.46

and the hole and ionic conduction are the dominant conduction mechanisms. In particular at low frequency, the increase in the dielectric constant and loss tangent is due to space charge polarization and ionic conductivity.⁴⁵ Moreover, the dielectric properties of BNT-6BT films can be effectively improved by increasing the thickness of the films, since ϵ_r of the films increases and $\tan \delta$ decreases. The 950 nm film shows the maximum value of ϵ_r (572) and the minimum value of $\tan \delta$ (0.032) at 1 kHz. It is well known that the dielectric response of ferroelectric film is affected by the microstructure and grain size, where films with larger grain size have higher ϵ_r and lower $\tan \delta$. In thicker films, the motion of the domain wall and domain switching are easier due to the larger grain size and domain size, leading to an increase in ϵ_r . In contrast, in small-grained films, grain boundaries are greatly increased, resulting in domain walls that can trap space charges.⁴⁶

It is well known that ϵ_r is proportional to the slope of the ferroelectric polarization–electric field (P – E) hysteresis loop at a certain electric field. The RT P – E hysteresis loops of BNT-6BT films with various thicknesses

were measured under 250 kV/cm at 1 kHz, and the results are shown in Fig. 9a. The corresponding variation in the maximum polarization (P_{max}) and remanent polarization (P_r) are shown in Fig. 9b and tabulated in Table I. The BNT-6BT films with the thickness of 450 nm, 600 nm, and 950 nm show saturation P – E hysteresis loops under 250 kV/cm, while the 300 nm film is unsaturated shape of that. Furthermore, the rounded P – E hysteresis loop of the 450 nm film with larger P_r and E_c is clearly observed, which indicates the significant contribution of leakage currents to the polarization. At the critical thickness of 450 nm, various defects will appear at the initial stage of columnar crystal growth, such as oxygen vacancies, which can pin ferroelectric domains and cause large leakage. Generally, the polarization properties of ferroelectric films are mainly derived from the asymmetry of the internal lattice and the motion and switching of the external domain wall.^{47,48} For BNT-6BT thin films, the existence of columnar crystals greatly increases the grain size along the film normal direction due to the effective release of mechanical strain. On the other hand, of particular importance is that the P_{max} increases with the film thickness, which may be due to the increased grain size of BNT-6BT films. The grain size increases with the film thickness, and the films transform into the multi-domain state, resulting in easier domain wall motion and domain switching.¹⁶ In addition, all the P – E hysteresis loops exhibit a slight shift toward the positive electric field. The horizontal offset of loops may occur for two reasons: one is the nonequivalence between the Pt bottom electrode and Au top electrode,⁴⁹ and the other is the presence of a built-in electric field originating from the defect dipoles during the film deposition process.⁵⁰

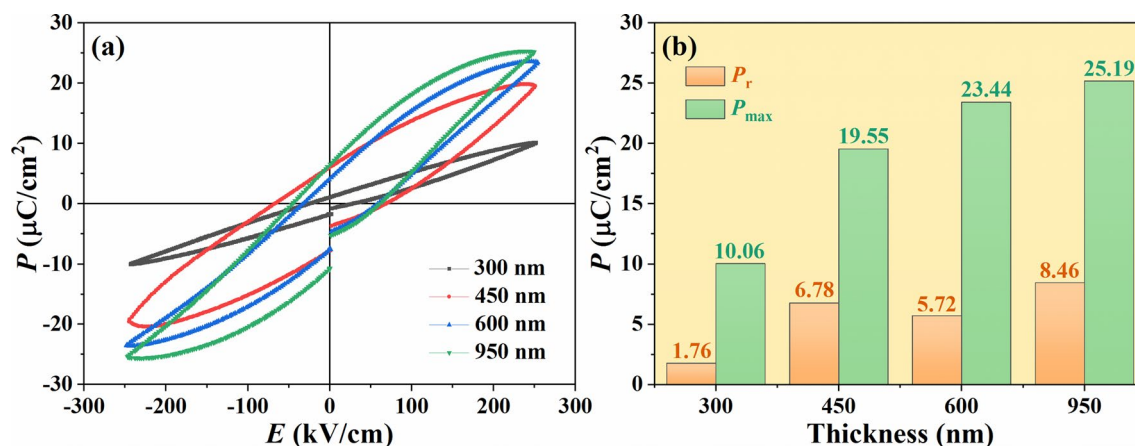


Fig. 9 (a) The RT P - E hysteresis loops of BNT-6BT films with various thicknesses under 250 kV/cm at 1 kHz, and (b) P_{\max} and P_r as a function of thickness.

Conclusions

In conclusion, BNT-6BT thin films with various thicknesses were deposited on Pt(111)/Ti/SiO₂/Si(100) substrates by PLD. The thickness-dependent structure, morphology, and dielectric and ferroelectric properties of the BNT-6BT films were systematically investigated. Polycrystalline films with a pseudo-cubic structure were obtained. With increasing thickness of the films, an increase in crystallinity and grain size, a decrease in strain, and the appearance of columnar crystals were realized. The obvious aging phenomenon with abnormal double-butterfly ϵ_r - E curves was observed in aged BNT-6BT films. The calculated dielectric tunability increased gradually with increasing film thickness, reaching a maximum value of 36.7%. Furthermore, an enhanced dielectric constant of 572 and dielectric loss of 0.032 were observed at 1 kHz for 950 nm film, and P_{\max} and P_r increased with film thickness, indicating the potential application of BNT-6BT films in film capacitors.

Acknowledgments This work was supported by the Guangxi Science and Technology Project (Grant No. AD21075033), the National Natural Science Foundation of China (Grant No. 52261005), and the Program for Bagui Scholars of Guangxi, China.

Conflict of interest The authors declare that they have no conflict of interest.

References

- G.A. Smolenski, V.A. Isupov, A.I. Agranovskaya, and N.N. Krainik, New ferroelectrics of complex composition IV. *Sov. Phys. Solid State* 2, 2651 (1961).
- T. Takenaka, K. Maruyama, and K. Sakata, (Bi_{1/2}Na_{1/2})TiO₃-BaTiO₃ system for lead-free piezoelectric ceramics. *Jpn. J. Appl. Phys.* 30, 2236 (1991).
- X.C. Huang, S. Li, C.C. Wang, H.J. Long, P.F. Chen, F.Y. Xiao, and Y.X. Chen, Structural, dielectric, and ferroelectric properties of BaTiO₃-Bi(Ni_{1/2}Ti_{1/2})O₃ lead-free ceramics with remarkable energy storage performance under low electric fields. *J. Mater. Sci. Mater. Electron.* 33, 10042 (2022).
- P. Parjansri, M. Kamnony, and S. Eitssayeam, Electrical properties of lead-free (Bi_{0.5}Na_{0.5})TiO₃ piezoelectric ceramics induced by BNT nanoparticles. *J. Electron. Mater.* 51, 1068 (2022).
- K.L. Zou, Y. Dan, H.J. Xu, Q.F. Zhang, Y.M. Lu, H.T. Huang, and Y.B. He, Recent advances in lead-free dielectric materials for energy storage. *Mater. Res. Bull.* 113, 190 (2019).
- Y. Mendez-González, A. Ferri, E.C. Lima, A. Hamieh, D. Remiens, A. Peláiz-Barranco, A.C. Silva, and J.D.S. Guerra, Structural and microstructural features of lead-free BNT-BT thin films: nanoscale electromechanical response analysis. *J. Am. Ceram. Soc.* 104, 3665 (2021).
- S. Pattipaka, J.P. Goud, G.P. Bharti, K.C.J. Raju, A. Khare, and D. Pamu, Effect of oxygen partial pressure on nonlinear optical and electrical properties of BNT-KNNG composite thin films. *J. Mater. Sci. Mater. Electron.* 31, 2986 (2020).
- Z. Zhou, S.W. Zhang, Y. Zhang, J. Luo, W. Sun, X.P. Wang, and J.F. Li, Textured Bi_{1/2}Na_{1/2}TiO₃-BaTiO₃ lead-free films with enhanced piezoelectric property and depolarization temperature. *Adv. Electron. Mater.* 4, 1800351 (2018).
- F.J. Chen, H. Qian, X.Y. Sun, M. Song, Y.F. Liu, and Y. Lyu, Grain size engineering and growth mechanism in hydrothermal synthesis of Bi_{0.5}Na_{0.5}TiO₃ thin films on Nb-doped SrTiO₃ substrates. *J. Sol-Gel Sci. Technol.* 99, 366 (2021).
- S. Pattipaka, P. Dobbidi, J.P. Goud, K.C.J. Raju, G. Pradhan, and V. Sridhar, Investigation of surface scaling, optical and microwave dielectric studies of Bi_{0.5}Na_{0.5}TiO₃ thin films. *J. Mater. Sci. Mater. Electron.* 33, 8893 (2022).
- Y.X. Li, Z.C. Wang, J.J. Yao, T.N. Yang, Z.G. Wang, J.M. Hu, C.L. Chen, R. Sun, Z.P. Tian, J.F. Li, L.Q. Chen, and D. Viehland, Magnetolectric quasi-(0-3) nanocomposite heterostructures. *Nat. Commun.* 6, 6680 (2015).
- P. Verardi, F. Craciun, N. Scarisoreanu, M. Dinescu, C. Grigoriu, and C. Galassi, Ferroelectric relaxor thin films grown by pulsed laser deposition. *Ferroelectrics* 293, 189 (2003).

13. S. Li, J.A. Eastman, Z. Li, C.M. Foster, R.E. Newnham, and L.E. Cross, Size effects in nanostructured ferroelectrics. *Phys. Lett. A* 212, 341 (1996).
14. M. Melo, E.B. Araújo, V.V. Shvartsman, V.Y. Shur, and A.L. Kholkin, Thickness effect on the structure, grain size, and local piezoresponse of self-polarized lead lanthanum zirconate titanate thin films. *J. Appl. Phys.* 120, 054101 (2016).
15. Q. Zhao, D. Su, M. Cao, G. He, J. Di, J. Yuan, and D. Wang, Thickness-dependent electrical properties of sol-gel derived $\text{Pb}(\text{Zr}_{0.52}\text{Ti}_{0.48})\text{O}_3$ thick films using PbTiO_3 buffer layers. *J. Mater. Sci. Mater. Electron.* 24, 3521 (2013).
16. W. Sun, J.F. Li, F.Y. Zhu, Q. Yu, L.Q. Cheng, and Z. Zhou, Thickness-dependent phase boundary in Sm-doped BiFeO_3 piezoelectric thin films on Pt/Ti/SiO₂/Si substrates. *Phys. Chem. Chem. Phys.* 17, 19759 (2015).
17. D.H. Kuang, P. Tang, S.H. Yang, and Y.L. Zhang, Thickness dependent ferroelectric and magnetic properties of $\text{Bi}_{0.9}\text{Gd}_{0.1}\text{Fe}_{0.9}\text{Co}_{0.1}\text{O}_3$ films prepared by RF magnetron sputtering. *J. Magn. Magn. Mater.* 397, 33 (2016).
18. F.J. Geng, C.H. Yang, C. Feng, P.P. Lv, X.M. Jiang, Q. Yao, Q. Zhang, C. Wei, and P. Song, Effects of single-coated layer thickness on the microstructure, leakage current and dielectric tunability of $\text{Na}_{0.5}\text{Bi}_{0.5}(\text{Ti}, \text{Zn})\text{O}_{3-\delta}$ thin films prepared by metal organic decomposition. *J. Alloys Compd.* 663, 659 (2016).
19. H.Y. Lee, L.S. Liu, J. Luo, Z. Zhen, and J.F. Li, Thickness-dependent switching behavior of $0.8(\text{Bi}_{0.5}\text{Na}_{0.5})\text{TiO}_3\text{-}0.2\text{SrTiO}_3$ lead-free piezoelectric thin films. *Ceram. Int.* 45, 16022 (2019).
20. S. Pattipaka, A. Joseph, G.P. Bharti, K.C.J. Raju, A. Khare, and D. Pamu, Thickness-dependent microwave dielectric and nonlinear optical properties of $\text{Na}_{0.5}\text{Bi}_{0.5}\text{TiO}_3$ thin films. *Appl. Surf. Sci.* 488, 391 (2019).
21. L. Kumar, P. Kumar, A. Narayan, and M. Kar, Rietveld analysis of XRD patterns of different sizes of nanocrystalline cobalt ferrite. *Int. Nanolett.* 3, 8 (2013).
22. A. Das, A.K. Chikkala, G.P. Bharti, R.R. Beher, R.S. Mamilla, A. Khare, and P. Dobbidi, Effect of thickness on optical and microwave dielectric properties of hydroxyapatite films deposited by RF magnetron sputtering. *J. Alloys Compd.* 739, 729 (2018).
23. D.G. Schlom, L. Chen, C. Eom, K.M. Rabe, S.K. Streiffer, and J. Triscone, Strain tuning of ferroelectric thin films. *Annu. Rev. Mater. Res.* 37, 589 (2007).
24. J. Hwang, Z. Feng, N. Charles, X.R. Wang, D. Lee, K.A. Stoerzinger, S. Muy, R.R. Rao, D. Lee, R. Jacobs, D. Morgan, and Y. Shao-Horn, Tuning perovskite oxides by strain: electronic structure, properties, and functions in (electro)catalysis and ferroelectricity. *Mater. Today* 31, 100 (2019).
25. C.Y. Deng, Y. Zhang, J. Ma, Y.H. Lin, and C.W. Nan, Magnetic-electric properties of epitaxial multiferroic $\text{NiFe}_2\text{O}_4\text{-BaTiO}_3$ heterostructure. *J. Appl. Phys.* 102, 074114 (2007).
26. A.K. Zak, W.H. Abd, M.E. Majid, and R.Y. Abrishami, X-ray analysis of ZnO nanoparticles by Williamson-Hall and size-strain plot Methods. *Solid State Sci.* 13, 251 (2011).
27. S.H. Wu, P. Chen, J.W. Zhai, B. Shen, P. Li, and F. Li, Enhanced piezoelectricity and energy storage performances of Fe-doped BNT-BKT-ST thin films. *Ceram. Int.* 44, 21289 (2018).
28. H. Brune and K. Kern, Heteroepitaxial metal growth: the effects of strain. *Chem. Phys. Solid Surf.* 8, 149 (1997).
29. X. Liu, S.D. Xue, F. Li, J.P. Ma, J.W. Zhai, B. Shen, F.F. Wang, X.Y. Zhao, and H.X. Yan, Giant electrostrain accompanying structural evolution in lead-free NBT-based piezoceramics. *J. Mater. Chem. C* 6, 814 (2018).
30. M.K. Niranjan, T. Karthik, S. Asthana, J. Pan, and U.V. Waghmare, Theoretical and experimental investigation of Raman modes, ferroelectric and dielectric properties of relaxor $\text{Na}_{0.5}\text{Bi}_{0.5}\text{TiO}_3$. *J. Appl. Phys.* 113, 194106 (2013).
31. S.H. Wu, B.J. Song, P. Li, B. Shen, and J.W. Zhai, Revealing the relationship between morphotropic phase boundary and tolerance factor of $\text{Na}_{0.5}\text{Bi}_{0.5}\text{TiO}_3$ -based thin films. *J. Eur. Ceram. Soc.* 40, 2954 (2020).
32. H. Lidjici, B. Lagoun, M. Berrahal, M. Rguitti, M.A. Hentatti, and H. Khemakhem, XRD, Raman and electrical studies on the $(1-x)(\text{Na}_{0.5}\text{Bi}_{0.5})\text{TiO}_3\text{-xBaTiO}_3$ lead free ceramics. *J. Alloys Compd.* 618, 643 (2015).
33. F.X. Yan, K. Han, G.Y. Zhao, X.J. Shi, N. Song, and Z.C. Jiao, Growth and magnetoelectric properties of (001)-oriented $\text{La}_{0.67}\text{Sr}_{0.33}\text{MnO}_3/\text{PbZr}_{0.52}\text{Ti}_{0.48}\text{O}_3$ heterostructure films. *Mater. Charact.* 124, 90 (2017).
34. Z. Cheng and Z. Zhao, Ink-jet printed BNT thin films with improved ferroelectric properties via annealing in wet air. *Ceram. Int.* 9, 10700 (2018).
35. J.J. Zhang, Y.F. Gao, X.R. Jia, J.Y. Wang, Z. Chen, and Y. Xu, Oxygen vacancy-rich mesoporous ZrO_2 with remarkably enhanced visiblelight photocatalytic performance. *Sol. Energy Mater. Sol. Cells* 182, 113 (2018).
36. J. Zhang, J. Zhai, and Y. Zhang, Correlations of dielectric properties with electronic structure and phonon vibration of low loss tunable $\text{Ba}_{0.4}\text{Sr}_{0.6}\text{Ti}_{1-y}\text{MnyO}_3$ ceramics. *J. Appl. Phys.* 110, 034105 (2011).
37. X.R. Jia, J.J. Zhang, L.J. Wang, J.Y. Wang, H.W. Du, Y.X. Yao, L.L. Ren, F. Wen, and P. Zheng, Role of oxygen-vacancy in piezoelectric properties and fatigue behavior of $(\text{Bi}_{0.5}\text{Na}_{0.5})_{0.93}\text{Ba}_{0.07}\text{Ti}_{1+x}\text{O}_3$ ceramics. *J. Am. Ceram. Soc.* 102, 5203 (2019).
38. P.P. Lv, C.H. Yang, F.J. Geng, C. Feng, X.M. Jiang, and G.D. Hu, Effect of defect dipole-induced aging on the dielectric property of Fe^{3+} -doped $\text{Na}_{0.5}\text{Bi}_{0.5}\text{TiO}_3$ thin film. *Ceram. Int.* 42, 2876 (2016).
39. J.H. Song, C.H. Yang, Q. Yao, Y.X. Zhang, C. Wei, and X.S. Sun, The microstructure, ferroelectric and dielectric behaviors of $\text{BiFeO}_3\text{-Na}_{0.5}\text{Bi}_{0.5}\text{TiO}_3$ based solid solution thin films. *Ceram. Int.* 43, 12287 (2017).
40. L.X. Zhang and X.B. Ren, Aging behavior in single-domain Mn-doped BaTiO_3 crystals: implication for a unified microscopic explanation of ferroelectric aging. *Phys. Res. B* 73, 094121 (2006).
41. W.L. Warren, G.E. Pike, K. Vanheusden, D. Dimos, B.A. Tuttle, and J. Robertson, Defect-dipole alignment and tetragonal strain in ferroelectrics. *J. Appl. Phys.* 79, 9250 (1996).
42. C.M. Folkman, S.H. Baek, C.T. Nelson, H.W. Jang, T. Tybell, X.Q. Pan, and C.B. Eom, Study of defect-dipoles in an epitaxial ferroelectric thin film. *Appl. Phys. Lett.* 96, 052903 (2010).
43. M.M. Ahmad, K. Yamada, P. Meuffels, and R. Waser, Aging-induced dielectric relaxation in barium titanate ceramics. *Appl. Phys. Lett.* 90, 112302 (2007).
44. Y. Li, Y.S. Wen, and X.Q. Feng, Effects of electric fatigue on the butterfly curves of ferroelectric ceramics. *Mater. Sci. Eng. A* 459, 273 (2007).
45. N. Scarisoreanu, F. Craciun, V. Ion, S. Birjega, and M. Dinescu, Structural and electrical characterization of lead-free ferroelectric $\text{Na}_{1/2}\text{Bi}_{1/2}\text{TiO}_3\text{-BaTiO}_3$ thin films obtained by PLD and RF-PLD. *Appl. Surf. Sci.* 254, 1292 (2007).
46. F. Xu, S. Trolier-McKinstry, W. Ren, and B.M. Xu, Domain wall motion and its contribution to the dielectric and piezoelectric properties of lead zirconate titanate films. *J. Appl. Phys.* 89, 1336 (2001).
47. L. Jin, F. Li, and S.J. Zhang, Decoding the fingerprint of ferroelectric loops: comprehension of the material properties and structures. *J. Am. Ceram. Soc.* 97, 1 (2014).
48. Y.Q. Gong, H.Y. Chen, S.H. Xie, and X.J. Li, Effects of Nb content on the ferroelectric and dielectric properties of Nb/Nd-Codoped $\text{Bi}_4\text{Ti}_3\text{O}_{12}$ thin films. *J. Electron. Mater.* 47, 1792 (2018).

49. M.M. Hejazi and A. Safari, Temperature-dependent leakage current behavior of epitaxial $\text{Bi}_{0.5}\text{Na}_{0.5}\text{TiO}_3$ -based thin films made by pulsed laser deposition. *J. Appl. Phys.* 110, 103710 (2011).
50. M. Bousquet, L. Batista, J.L. Dellis, A. Boule, U. Rabe, O. Durand-Drouhin, Y. Gagou, L. Dupont, V. Viallet, A. Zeinert, S. Hirsekorn, and N. Lemée, Structural and electrical properties of $\text{Bi}_{0.5}\text{Na}_{0.5}\text{TiO}_3$ based superlattices grown by pulsed laser deposition. *J. Appl. Phys.* 116, 194104 (2014).

Springer Nature or its licensor (e.g. a society or other partner) holds exclusive rights to this article under a publishing agreement with the author(s) or other rightsholder(s); author self-archiving of the accepted manuscript version of this article is solely governed by the terms of such publishing agreement and applicable law.

Publisher's Note Springer Nature remains neutral with regard to jurisdictional claims in published maps and institutional affiliations.